Microstructure, thermo-mechanical properties and Portevin-Le Chatelier effect in metastable β Ti-xMo alloys

S. Luo, P. Castany, S. Thuillier

▶ **To cite this version:**

HAL Id: hal-02122158
https://univ-rennes.hal.science/hal-02122158

Submitted on 18 Jul 2019

Microstructure, thermo-mechanical properties and Portevin-Le Chatelier effect in metastable β Ti-*x*Mo alloys

Shiyuan Luo[a, *], Philippe Castany[b], Sandrine Thuillier[a]

[a] *Univ. Bretagne Sud, UMR CNRS 6027, IRDL, F-56100 Lorient, France*

[b] *Univ Rennes, INSA Rennes, CNRS, ISCR-UMR 6226, F-35000 Rennes, France*

Abstract

The microstructure, mechanical properties and Portevin-Le Chatelier (PLC) effect in Ti-*x*Mo alloys (*x*=10, 12, 15 and 18 wt%), in the temperature range of 250-350 °C with strain rates from 10^{-3} s^{-1} to 10^{-4} s^{-1}, are systematically investigated in tension by using transmission electron microscopy and Gleeble 3500 testing machine combined with a digital image correlation technique. Results show that Young modulus decreases with increasing Mo contents, which is related to a more stable β phase matrix and a decrease of ω phase fraction. Moreover, the values of Young modulus and 0.2% offset yield strength at elevated temperature are higher than the ones at room temperature in all the Ti-*x*Mo alloys, except the Ti-18Mo alloy which shows an opposite result. These macroscopic features are consistent with the ω phase precipitation in deformed Ti-*x*Mo alloys, due to the combined effects of ω phase strengthening and temperature softening. Furthermore, the serration type transforms from A to A+B, then to B and eventually to C as increasing temperature and decreasing strain rate as well as Mo contents, which mainly depends on the spatial cohesion of PLC bands influenced by the intensity of ω precipitate-dislocation interactions. Finally, the peak value of maximum stress drop magnitude appears in Ti-12Mo alloy and increases with decreasing the strain rate, which is attributed to a stronger intensity of ω precipitate-dislocation interactions caused by reducing dislocations movement and

* Corresponding author. Tel.: +86 15927422692. E-mail address: sy-luo@foxmail.com (S.Y. Luo)

providing a longer ageing time for the precipitation of ω phase particles. Besides, the average stress drop magnitude increases in Ti-18Mo alloy and decreases in the other compositions as increasing engineering strain, which is related to the variation of ω phase fraction.

Keywords: β titanium alloys, Mo content, Thermo-mechanical behavior, Portevin-Le Chatelier effect, Digital image correlation, Transmission electron microscopy

1. Introduction

Titanium alloys are extensively used in many applications from biomedical devices to aeronautics, owing to their good strength-to-weight ratio, high corrosion resistance, enhanced hardenability and excellent biocompatibility [1-4]. Focusing on metallic biomaterials, much effort has been devoted to investigating the β titanium alloys made of nontoxic elements [5-8], especially employing Mo alloying element [9-11]. This is mainly attributed to the fact that molybdenum, as an effective β stabilizer, is less toxic than other alloying elements, and it can be used to develop titanium alloys with a high strength and low elastic modulus suitable for implant applications [12]. However, Portevin-Le Chatelier (PLC) effect, as a type of plastic instability, is found in Ti-15Mo alloys under thermo-mechanical loading conditions [13]. Hence, for a practical use of these materials, the investigation of PLC effect in Ti-xMo alloys becomes an urgent demand, as such an effect severely influences the plastic behavior and mechanical properties.

Until now, some fundamental studies related to the microstructure have been performed on binary Ti-xMo alloys. After a solution heat treatment followed by water quenching, three different metastable phases can be observed in the β phase matrix, which are hexagonal martensite α′ [14], orthorhombic

martensite α″ [15] and athermal ω_{ath} [16]. Based on different Mo contents, these phases are respectively formed by β → α′ (0 < x ≤ 6 wt%), β → α″ (6 < x ≤ 8 wt%), and β → ω_{ath} (x > 8 wt%) phase transformations [17]. Moreover, several studies reported that the amount of ω_{ath} phase formed in Ti-xMo alloys (10 ≤ x ≤ 20 wt%) is the highest for Mo contents lying between 10 and 12 wt% and decreases as increasing Mo content [18-20]. Furthermore, Zhou et al. [21] investigated the effect of deformation on the microstructural evolution in Ti-10Mo alloy, and results showed that α″ phase is also formed after cold rolling process due to the stress-induced β → α″ transformation. Sun et al. [22] investigated the microstructural evolution of Ti-12Mo alloy during uniaxial tensile tests at room temperature and found stress-induced α″ phase at early deformation stage by using in situ synchrotron X-ray diffraction (SXRD) and transmission electron microscopy (TEM). Apart from observations at room temperature, Cardoso et al. [23] investigated the microstructural evolution of Ti-xMo alloys (3 ≤ x ≤ 15 wt%) during isothermal ageing heat treatment and discovered that isothermal phase (ω_{iso}) is formed by β → ω_{iso} transformation as Mo content exceeds 7.5 wt%. However, very few information on this precipitation kinetics is reported, except some studies using electrical resistivity and dilatometry measurements [24-26]. They mainly show that the nucleation of ω_{iso} is almost instantaneous and the kinetics of growth increases with the temperature. But, to the authors' knowledge, there is no report on the effect of composition on precipitation kinetics.

For the mechanical properties of Ti-xMo alloys, a better understanding of the relationship between microstructure and mechanical properties is essential. Zhang et al. [27] studied the elastic modulus (E) of different phases in binary Ti-xMo alloys and observed that $E_{\omega} > E_{\alpha'} > E_{\alpha''} > E_{\beta}$. Consequently, E values are found to be the highest for 10 < x < 13 wt% [28] because the ω_{ath} volume fraction is the highest in this range of compositions. Conversely, E value decreases as x ≥ 13 wt% due to the reduction

of ω_{ath} phase, and as $x \leq 10$ wt%, which is attributed to the precipitation of α'' phase instead of ω_{ath}

phase [20]. Moreover, Lee et al. [29] investigated the microhardness (H) of different phases in Ti-based

alloys, and results indicated that $H_\omega > H_{\alpha'} > H_{\alpha''} > H_\beta$. The evolution of H values in Ti-xMo alloys ($7.5 \leq$

$x \leq 20$ wt%) show that the largest value appears in Ti-12.5Mo alloy, stemming from a relatively large

fraction of ω phase particles [20]. Furthermore, it is well established that the precipitation of ω phase in

β phase matrix can significantly enhance the mechanical strength of Ti-xMo alloys, though it also leads

to embrittlement and subsequent loss of ductility [30-32]. It is worth noting that, although the above

studies have been performed to investigate mechanical properties at room temperature, none of them is

directly related neither to the thermo-mechanical behavior nor to PLC effect.

PLC effect, also referred as serrated yielding or jerky flow, is caused by the repetitive arresting

and releasing of mobile dislocations during deformation [33]. Up to now, a large number of studies

have been carried out on the mechanism of PLC effect in various alloy systems. Zhong et al. [34]

reported that the solute element Mg is responsible for the generation of PLC effect in Al-Mg alloys,

while Cai et al. [35] considered γ' precipitates as obstacles to account for this effect in Ni-based alloys.

Moreover, Zhou et al. [36] suggested that PLC effect in steels results from the diffusing

atom-dislocation interactions. Furthermore, for α-Ti alloys, Prasad et al. [37] discovered that PLC

effect is attributed to the interactions between interstitial elements and mobile dislocations. Unlike α-Ti

alloys, Banerjee et al. [13] proposed that the jerky flow is caused by ω precipitate-dislocation

interactions in Ti-15Mo alloys. It can be noted that the mechanism for the generation of PLC effect in

various alloy systems is non-unique.

Moreover, significant attention has been paid to the spatiotemporal characteristics of PLC effect.

Focusing on the temporal aspect, researchers classified the serrated flow into three types (A, B and C)

4

depending on the characteristics of serration morphologies [38-40]. Amokhtar et al. [41] investigated serration type and stress drop magnitude in Al-based alloys, and found that stress drop magnitude increases and serration type transforms from type B to C with increasing Mg contents. The number of stress drops per unit time in Al-Mg alloys is also inversely proportional with Mg contents [42], while the critical strain for the generation of PLC effect is proportional to Mg contents [43]. Furthermore, Niu et al. [44] studied the effects of temperature and strain rate on serration type in $Al_{0.5}CoCrFeNi$ high entropy alloy, and results showed that serration type transforms from A to A+B and then to B+C when increasing temperature and decreasing strain rate. Concerning the spatial aspect, bands of localized deformation (PLC bands), associated to the jerky flow, are generally classified as type A-continuous propagation [45], type B-hopping propagation [46] and type C-random nucleation [47]. The band propagation is usually observed by four methods including digital image correlation (DIC) [48], digital speckle pattern interferometry [49], infrared thermography [50] and shadowgraph [51]. Casarotto et al. found that the required strain rate for type A is relatively higher in Al-3Mg (wt%) alloy than the one for type B [52]. Chihab et al. [53] studied three types of PLC bands, and results indicated that the required strain rate for the generation of type C PLC bands is the lowest in Al-5Mg (wt%) alloy. Yuzbekova et al. [54] found that the variation of propagation types in Al-3Mg alloy is also influenced by the lattice dislocation density and grain size. Additionally, Shabadi et al. [55] found that the width of PLC band increases and then tends to stabilize as increasing strain in AA7020 alloy. Callahan et al. [56] reported that the propagation speed of PLC bands decreases linearly with strain in medium Mn steels.

Although a large number of studies on PLC effect has been carried out on steels [57-59], Al-Mg alloys [60-62], Ni-based superalloys [63-65] and Ti-based alloys [66-68], to date, it is less reported in metastable β Ti alloys. Hereinto, Banerjee et al. [13] only qualitatively investigated the plastic

instability in Ti-15Mo alloy within a range of temperatures and strain rates which ignored the influence

of Mo contents on PLC effect. Luo et al. [69] quantitatively studied the effect of temperature on the

number of stress drops per unit time and stress drop magnitude in Ti-12Mo and Ti-15Mo alloys.

However, none of the above studies is directly tied to the comprehensive analysis of the effects of Mo

contents and process parameters on microstructure, mechanical properties and PLC effect in Ti-xMo

alloys under thermo-mechanical environment. Therefore, in this paper, a series of Ti-xMo alloys (x =

10, 12, 15 and 18 wt%) are synthesized, and then tested in tension coupled with a DIC technique. These

tensile tests are carried out in the temperature range of 250-350 °C with strain rates from 10^{-3} s^{-1} to

10^{-4} s^{-1}. Subsequently, the tensile behavior of the synthesized Ti-xMo alloys is systematically

investigated and the microstructure of deformed Ti-xMo alloys is observed by TEM. Finally, the

influence of Mo contents and process parameters on mechanical properties and PLC effect in Ti-xMo

alloys is investigated qualitatively and quantitatively.

2. Materials and experimental procedures

Four Ti-xMo alloys (x=10, 12, 15 and 18 wt%) are synthesized by using cold crucible levitation

melting with pure molybdenum (99.99 wt%) and titanium (99.95 wt%) in a water-cooled Cu crucible

under Ar atmosphere. Then, the synthesized ingots undergo a homogenization heat treatment at the

temperature of 950 °C for 20 hours followed by water quenching, and the surface oxide layers are

removed in a mixed acidic (50 vol% HNO3 and 50 vol% HF) bath. Thereafter, the ingots are rolled into

1 mm thickness sheets (about 90% reduction in thickness) and tensile samples are machined along the

rolling direction using a $15 \times 3 \times 1$ mm^3 gauge size, as presented in Fig. 1(a). Finally, the samples are

subjected to a recrystallization heat treatment at the temperature of 870 °C for 0.5 hour followed by

water quenching. The actual chemical compositions of water-quenched Ti-xMo alloys are measured by

EDS-SEM (Energy Dispersive X-Ray Spectrometry in Scanning Electron Microscope). Average values in weight percent for 5 different areas per alloy are given in Table 1. Besides, the microstructure of water-quenched tensile samples is analyzed by optical micrographs (OM) and X ray diffraction (XRD) with Cu Kα1 radiation (λ = 0.154060 nm) using a Philips PW3710 diffractometer. Note that the details of OM sample preparation processes are described by Luo et al. [69]. Figs. 1(b) and (c) show the diffractograms and optical micrographs, respectively. It is observed that retained β phase is the dominant phase and recrystallized equiaxial grains are formed after the whole elaboration process.

Table 1

Average chemical compositions of the Ti-xMo alloys and mean square deviations (wt%)

Alloy	Ti	Mo	Mean square deviation
Ti-10Mo	89.93	10.07	± 0.16
Ti-12Mo	87.85	12.15	± 0.17
Ti-15Mo	85.19	14.81	± 0.22
Ti-18Mo	82.13	17.87	± 0.26
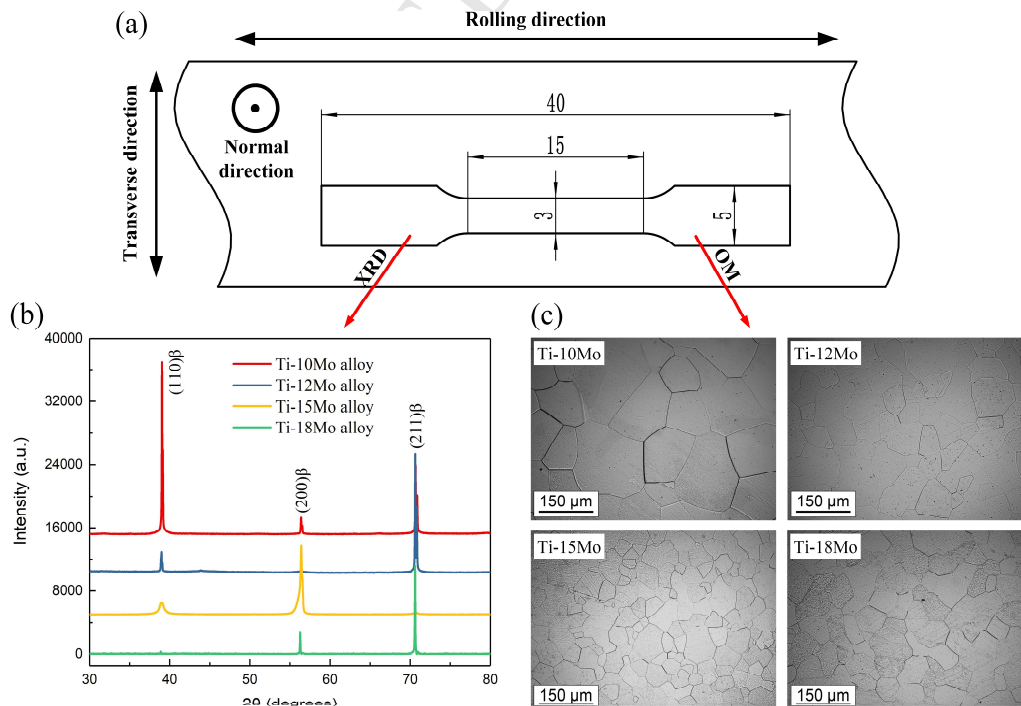
Fig. 1. Sample size (a), XRD (b) and OM (c) observations of Ti-xMo alloys.

Subsequently, tensile tests are conducted on Gleeble 3500 testing machine coupled with DIC (Aramis) in the temperature range of 250 °C-350 °C and strain rates ranging from 10^{-3} s^{-1} to 10^{-4} s^{-1}, as shown in Fig. 2(a). Moreover, the partial enlarged detail of tensile sample sprayed with a random pattern of black dots over a white background is shown as inset in the lower left corner. Prior to tensile tests, using a heating rate of 10 °C s^{-1}, samples are heated to 250 °C or 350 °C followed by holding under isothermal conditions during 10 s. The strain field is measured continuously on the specimen surface by two digital cameras with a rate of 10 frames per second, and the fluctuations of temperature are maintained within 2 °C until rupture. Furthermore, two half contact AISI 304 stainless steel grips are employed to hold tensile samples instead of the full contact copper grips used in [69], thereby leading to a much smaller temperature gradient along the tensile direction during the whole test. Thus, a relatively larger area at the specimen center with a length of 10 mm is chosen to observe PLC effect, where the temperature heterogeneity is less than 11.2%, as shown in Fig. 1(b). It should be pointed out that repeated tests (at least twice) are performed under all of designated experimental conditions to ensure the reproducibility of the results. After the tests, through coupling the data from the tensile testing machine and Aramis software by a linear interpolation method, the load-time curves and strain-time curves are turned to engineering stress-strain curves. Note that a 10 mm gauge length is used to calculate the engineering strain. In addition, Young modulus and 0.2% offset yield strength (YS) reported in this paper are the average values over two tests. For each test, Young modulus is calculated as the slope of the engineering stress-strain curve in the stress range [100-400 MPa]. Finally, the microstructure of deformed Ti-xMo alloys is observed by TEM with a Jeol 2100 machine operating at 200 kV. Samples are cut as 3 mm diameter disks and polished to a thickness of about 100 µm with SiC abrasive papers. Final thinning is made from twin-jet electropolishing using a 4 vol% perchloric acid

solution in methanol at -20 °C.
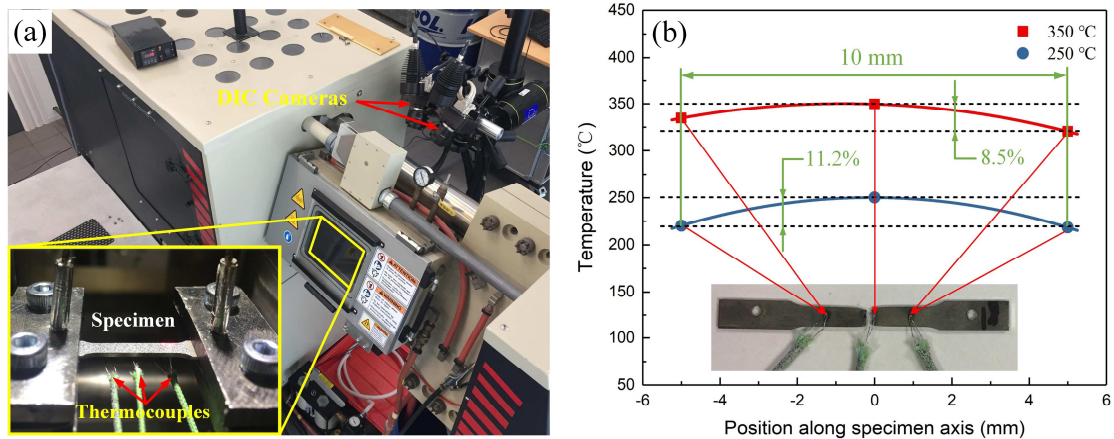
Fig. 2. Gleeble 3500 testing machine coupled with DIC for Ti-*x*Mo alloys tensile tests at elevated

temperatures (a) and temperature distribution along specimen axis (b).

3. Results

3.1 Engineering stress-strain curves

Fig. 3 presents the engineering stress-strain curves of Ti-*x*Mo alloys. For a better view, the partial

enlarged details of the curves are added in the lower right corner. Globally, the strain distribution is

rather heterogeneous due to PLC effect, and then tends to localize in one or two necking areas where

the logarithmic strain reaches maximum values in-between 0.32 and 0.72. Moreover, it can be seen

from Fig. 3 that the serrated flow appears for all elevated temperatures and the serration morphology

obviously changes with temperature, strain rate and Mo content. Furthermore, the stress level generally

increases with decreasing the strain rate at the same temperature.
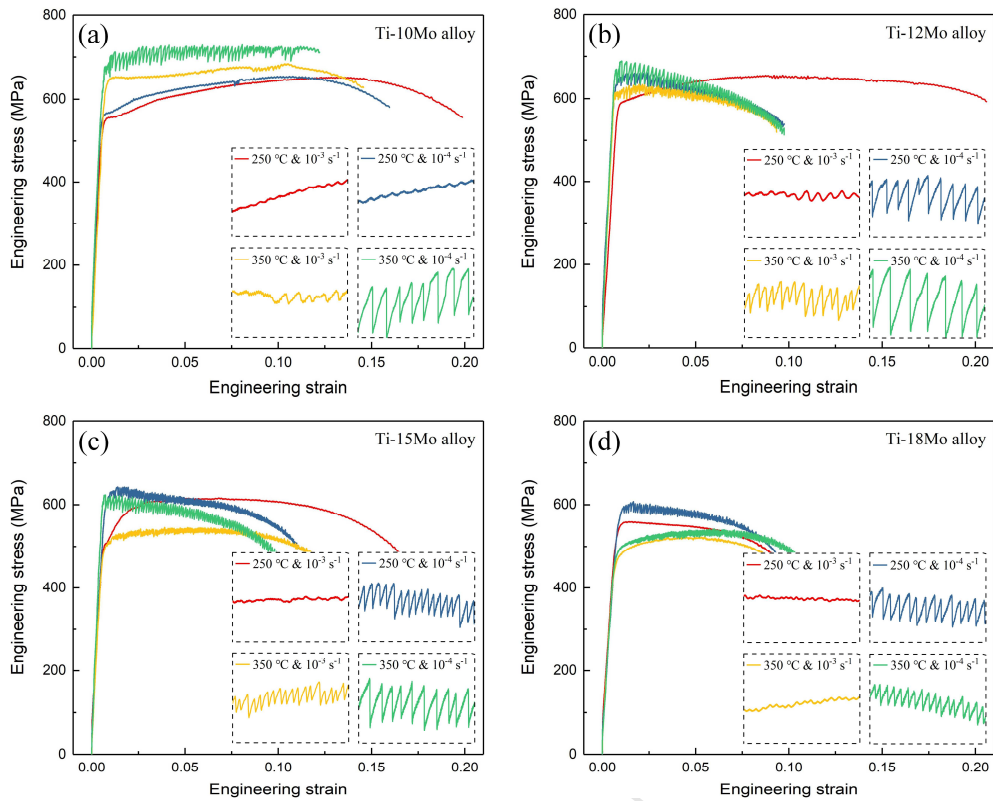
Fig. 3. Engineering stress-strain curves of Ti-xMo alloys at the temperature range of 250-350 °C with

strain rates from the order of 10^{-3} s^{-1} to 10^{-4} s^{-1}.

3.2 Propagation characteristics of PLC bands

Fig. 4 presents several typical propagation characteristics of PLC bands described by strain rate

maps, corresponding to different serration morphologies shown in Fig. 3. For a maximum contrast, an

independent color scale is employed for each frame and the corresponding time and maximum strain

rate are shown under and over each frame, respectively. It is observed from Fig. 4 that localized

deformation bands characterized by high strain rate appear at elevated temperatures in all Ti-xMo

alloys (x = 10, 12, 15 and 18 wt%), which is quite different from the homogeneous deformation pattern

of Ti-15Mo alloy at room temperature reported earlier by Luo et al. [69]. Figs. 4(a) shows a continuous

propagation characteristic of type A PLC bands, as time increases from 91.5 s to 100.5 s for the

experimental condition (250 °C & 10^{-3} s^{-1}). Unlike Fig. 4(a), it is observed from Fig. 4(b) that type B

PLC bands propagate along the gauge length in an intermittent manner, with roughly equal intervals,

for the experimental condition (350 °C & 10^{-4} s^{-1}). Moreover, a mixed propagation of type A+B, consisting of continuous and hopping propagations, is observed in Ti-12Mo alloy for the experimental condition (250 °C & 10^{-3} s^{-1}), as shown in Fig. 4(c). Besides, compared with Fig. 4(b), it can be observed from Fig. 4(d) that type C bands appear at random intervals along the gauge length in Ti-10Mo alloy for the experimental condition (350 °C & 10^{-4} s^{-1}). In general, the type of PLC bands is related to the spatial coupling force [69].
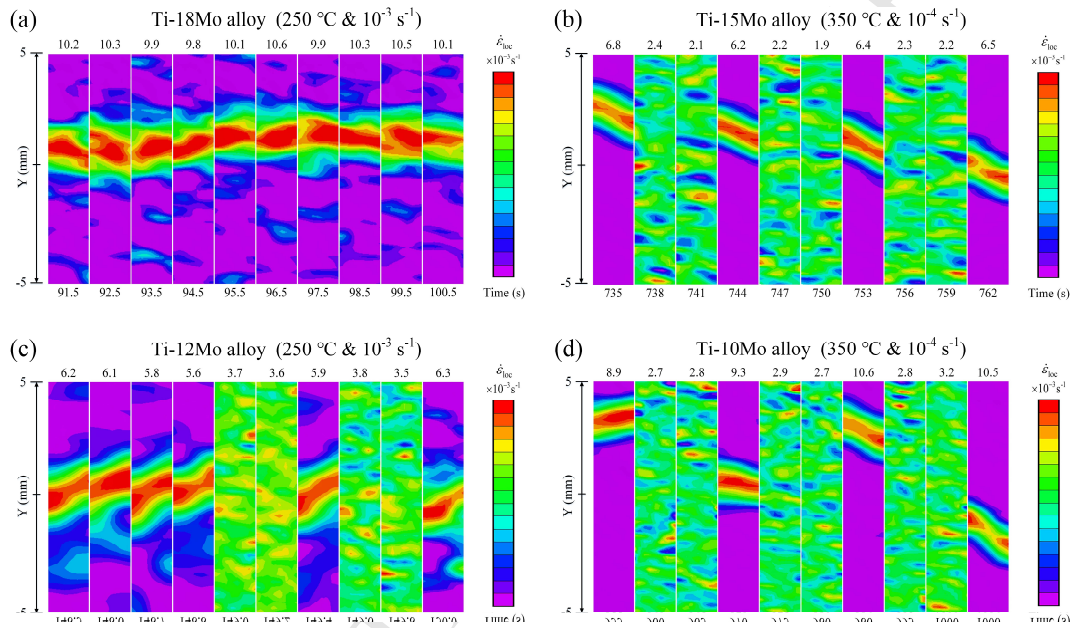
Fig. 4. Several typical propagation characteristics of PLC bands.

3.3 Microstructures

Figs. 5(a)-(d) show the $[113]_\beta$ selected area electron diffraction (SAED) patterns of Ti-xMo alloys (x=10, 12, 15 and 18 wt%), respectively, after a tensile deformation under the experimental condition (350 °C & 10^{-4} s^{-1}). It can be observed that a certain amount of ω_{iso} phase particles is formed in all Ti-xMo alloys after tension at elevated temperature. Moreover, as the ω reflection intensity is related to the phase volume fraction, it can be seen that the fraction of ω_{iso} phase particles in Ti-18Mo alloy (Fig. 5(d)) is the lowest among all the Ti-xMo alloys, by comparing the ω reflection intensity of each SAED pattern. Furthermore, Figs. 5(e) and (f) show the dark field TEM images of ω phase particles in

Ti-12Mo and Ti-18Mo alloys, respectively. It can be seen that the ω phase particle fraction of Ti-12Mo

alloy is much higher than the one of Ti-18Mo alloy, which confirms the SAED pattern information.

Besides, it can be found that the size of ω phase particles is very small (about 4-8 nm), which is highly

consistent to the observation reported by Gysler et al. [70], who found that the diameter of ω phase

particles in Ti-11Mo alloy is about 4-10 nm after ageing at 350 °C for various times.

Fig. 5. SAED patterns of Ti-10Mo (a), Ti-12Mo (b), Ti-15Mo (c) and Ti-18Mo (d) alloys as well as the

dark field TEM images taken with spots of ω phase of Ti-12Mo (e) and Ti-18Mo (f) alloys after tensile

deformation under the experimental condition (350 °C & 10^{-4} s^{-1}). The zone axis is parallel to $[113]_\beta$.

4. Discussion

4.1 Effects of Mo content and process parameters on mechanical properties

Fig. 6 shows the Young modulus and 0.2% offset yield strength (YS) of Ti-xMo alloys, calculated

from the curves presented in Fig. 3. It is observed from Fig. 6(a) that Young modulus obviously

decreases with increasing Mo contents under all the experimental conditions. As the Young modulus

value of β phase is the lowest among all the phases of Ti-xMo alloys [27], the above phenomenon can

be explained by a relatively higher Mo content, that renders the β phase matrix more stable and

decreases the precipitation ability of ω_{iso} phase. Moreover, for a fixed Mo content, it can be observed

from Fig. 6(a) that the difference between Young modulus values measured at elevated temperature and

the ones obtained at room temperature in the present work or in literature [19, 23, 71] changes from -10

GPa to 18 GPa as changing temperature and strain rate. This phenomenon can be attributed to the

combined influence of interatomic bonding energy and ω phase particles. Specifically, for Ti-10Mo

alloy, Young modulus (about 102 GPa) under the experimental condition (250 °C & 10^{-3} s^{-1}) is slightly

higher than the one at room temperature. Indeed, a high temperature contributes to the precipitation of

ω phase particles, and Young modulus value of ω phase is the highest of present phases in Ti-xMo

alloys [27]. Then, compared with the condition (250 °C & 10^{-3} s^{-1}), it can be found that Young modulus

value for the experimental condition (250 °C & 10^{-4} s^{-1}) is further increased. The main reason for this

trend, contrary to a classical viscoelastic dependence, is that during the tensile tests, the duration of

elastic stage increases from 82 s to 812 s when decreasing the strain rate from the order of 10^{-3} s^{-1} to

10^{-4} s^{-1}, leading to a longer ageing time, thereby leading to a higher fraction of ω precipitate particles.

In contrast, it can be observed that Young modulus value (about 95 GPa) under the experimental condition (350 °C & 10^{-3} s^{-1}) is lower than the one at room temperature. Indeed, a relatively higher temperature enlarges the interatomic distance resulting in a lower interatomic bonding energy, thereby leading to a reduction of Young modulus, which is not compensated by a high enough fraction of ω_{iso} phase. Furthermore, it can be found that Young modulus value (about 108 GPa) under the experimental condition (350 °C & 10^{-4} s^{-1}) is the highest among all the results of Ti-10Mo alloy. This is mainly because the combination of high temperature and long ageing time leads to the highest amount of ω_{iso} phase particles. The same trend is observed for Ti-12Mo and Ti-15Mo alloys. Compared with Ti-10Mo alloy, the variation ranges for Ti-12Mo and Ti-15Mo alloys are wider, which indicates that their Young modulus values are more sensitive to the change of temperature and strain rate. In addition, it can be observed that Young modulus values of Ti-18Mo alloy at all the elevated temperatures are lower than the one at room temperature. The main reason is that the fraction of ω_{iso} phase particles is lower due to the higher stability of the β phase, and thereby the effect of decreasing interatomic bonding energy is insufficiently compensated by the effect of ω_{iso} phase particles in Ti-18Mo alloy.

Unlike Young modulus, it can be observed from Fig. 6(b) that after a decrease, the YS sharply increases from the level of 439 MPa, when Mo content increases to 15 wt% at room temperature. This is attributed to the combined influence of ω phase particles and deformation mode. In Ti-*x*Mo alloys (10 ≤ x ≤ 15 wt%), the ability to form ω_{ath} phase is weakened by a relatively higher Mo content, thereby leading to a decrease of YS value. While, as Mo content excesses 15 wt%, the dramatic rise of YS value is mainly attributed to the change of deformation modes from twinning to slip, as evidenced for Ti-*x*Mo alloys (10 ≤ x ≤ 25 wt%) [72]. Moreover, the YS value also shows a significant variation with temperature and strain rate at a fixed Mo content, and the difference between the value at elevated

temperature and the one at room temperature changes from -308 MPa to 176 MPa (Fig. 6(b)). This is

attributed to a combination of the ω phase strengthening effect and temperature softening effect.

Furthermore, it can be observed from Ti-18Mo alloy that the highest value of YS at elevated

temperature is lower than the one at room temperature, which is opposite to the results for the other

three compositions, even though the average grain size of Ti-18Mo alloy is smaller than the ones of

Ti-10Mo and Ti-12Mo alloys, as shown in Fig. 1(c). The above phenomenon is consistent with the

observation of Young modulus, which also depends on the competition of ω_{iso} phase particle

strengthening effect and temperature softening effect. Contrary to the other three alloys, the softening

effect of temperature overcomes the strengthening effect of ω_{iso} phase in Ti-18Mo alloy due to a lower

ability to precipitate ω_{iso} phases in the β phase as shown in Fig. 5. Besides, the stress level presented in

Fig. 3 increases with decreasing the strain rate at the same temperature and Mo content. This feature

can be explained by the reason that a relatively lower strain rate can reduce dislocations movement and

enhance the precipitation of ω phase particles, resulting in a stronger capability for pinning dislocations,

thereby leading to the increase of the average stress level at the initial stage of deformation.
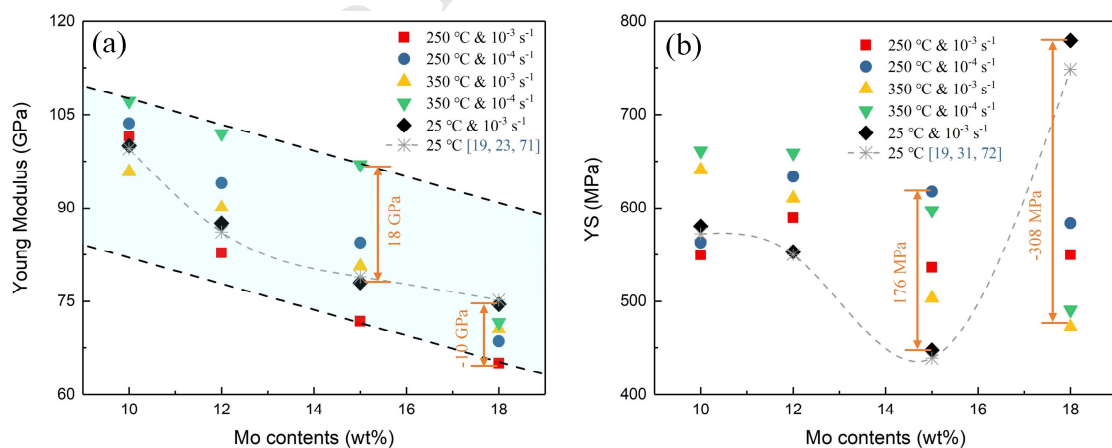
Fig. 6. Young modulus (a) and 0.2% offset yield strength (YS) (b) of Ti-*x*Mo alloys at the temperature

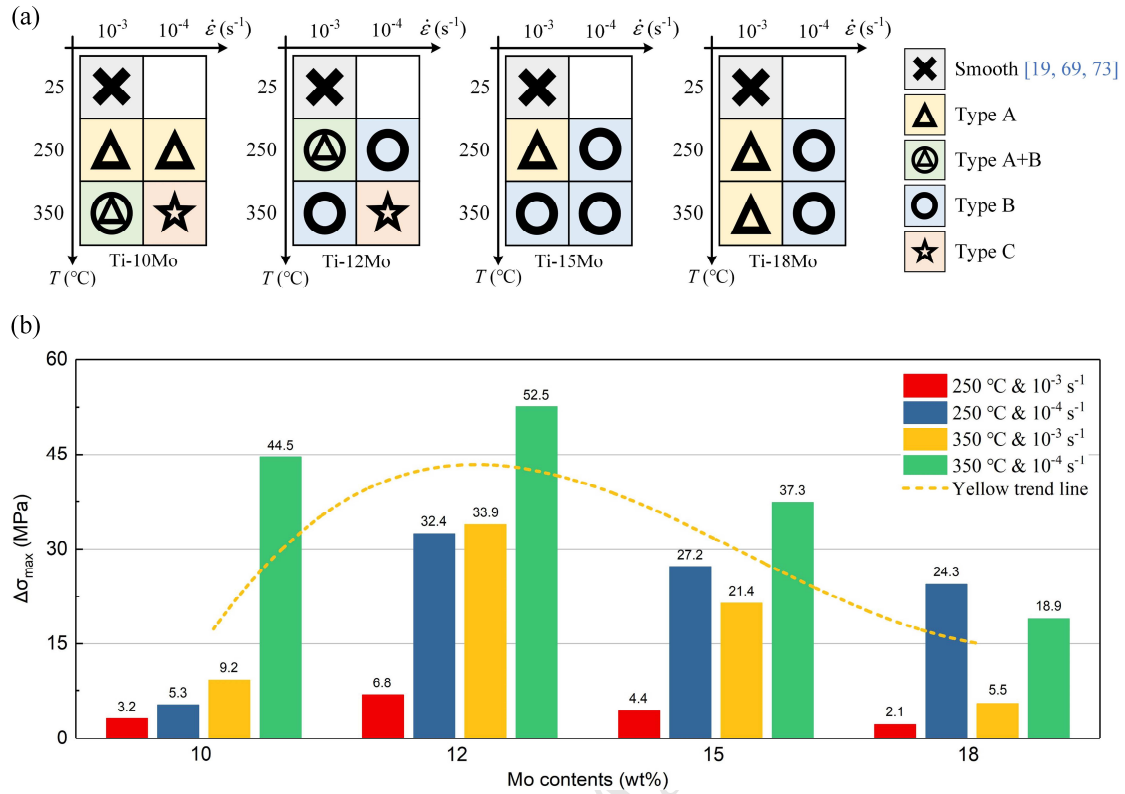range of 25-350 °C with strain rates from 10^{-3} s^{-1} to 10^{-4} s^{-1}.

4.2 Mechanism of serration morphology evolution

To qualitatively and quantitatively reveal the variations of serration morphology with temperature, strain rate and Mo content presented in Fig. 3, the summary of serration type and maximum stress drop magnitude ($\Delta\sigma_{max}$) under all the experimental conditions are presented in Fig. 7. It can be found from Fig. 7(a) that the serrated flow appears at all the elevated temperatures, which has been explained by the interactions between mobile dislocations and ω phase particles [13]. Specifically, ω phase particles formed during tensile process firstly pin mobile dislocations. Then, a stress drop occurs suddenly when the pinning ω precipitates are sheared by dislocations. Subsequently, the dynamic ω phase restoration occurs in ω-free soft channels created by dislocation avalanche, further resulting in a pinning of mobile dislocations, thereby leading to the increase of stress. Moreover, according to the classification method of serrated flow described by Pink [39], it can be observed from Fig. 7(a) that the serration type switches from A to A+B, then to B and eventually to C in Ti-*x*Mo alloys as changing temperature and strain rate, which indicates that the intensity of ω precipitate-dislocation interactions varies under different experimental conditions. For Ti-10Mo alloy, the serration type remains type A when decreasing strain rate from 10^{-3} s^{-1} to 10^{-4} s^{-1} at 250 °C. Indeed, although the ageing time increases about tenfold, the precipitation ability of ω phase particles is still limited during the tensile process, thereby leading to a weak ω precipitate-dislocation interactions at 250 °C. Moreover, it can be found that the serration type transforms from type A to A+B when the temperature increases from 250 °C to 350 °C and with a strain rate of order 10^{-3} s^{-1}, which is due to the higher fraction of ω phase particles caused by the temperature increase. This is supported by the investigation of Banerjee et al. [13], which also found that at a given strain rate, increasing temperature can result in a stronger intensity of ω precipitate-dislocation interactions. Then, keeping the temperature at 350 °C and decreasing the strain

16

down to 10^{-4} s^{-1}, it can be observed that the serration type further switches from type (A+B) to C in Ti-10Mo alloy. This is mainly because a relatively lower strain rate reduces dislocations movement and extends ageing time for the precipitation of ω phase particles, further enhancing ω phase-mobile dislocation interactions. Unlike Ti-10Mo alloy, type (A+B) is observed in Ti-12Mo alloy under the experimental condition (250 °C & 10^{-3} s^{-1}). This finding suggests that the ability to form ω phase particles in Ti-12Mo alloy is stronger than the one in Ti-10Mo alloy. Furthermore, such a transformation of the band type in Ti-12Mo alloy can be explained by the same reason as for Ti-10Mo alloy. However, the serration type of Ti-15Mo alloy for the experimental conditions (250 °C & 10^{-3} s^{-1} and 350 °C & 10^{-4} s^{-1}) are types A and B, respectively. This is mainly attributed to a weaker intensity of ω precipitate-dislocation interactions in Ti-15Mo alloy caused by a relatively higher Mo content. This view is fully supported by Banerjee et al. [13], who found that there is no jerky flow in Ti-25Mo alloy. In addition, it can be seen from Ti-18Mo alloy that the serration type changes from type A to B with the decrease of strain rate at both 250 °C and 350 °C. This finding suggests that the transformation of serration type is more sensitive to strain rate rather than temperature in Ti-18Mo alloy.

Moreover, it can be observed from Fig. 7(b) that $\Delta\sigma_{max}$ values show good agreement with serration types presented in Fig. 7(a), and they decrease gradually after a sharp increase when Mo content increases from 10 wt% to 12 wt%. Furthermore, $\Delta\sigma_{max}$ value increases as decreasing the strain rate from 10^{-3} s^{-1} to 10^{-4} s^{-1} for the same temperature, which is attributed to a stronger intensity of ω precipitate-dislocation interactions caused by a longer ageing time and lower speed of dislocations. Finally, it can be observed that the highest $\Delta\sigma_{max}$ value (52.5 MPa) appears under the experimental condition (350 °C & 10^{-4} s^{-1}) in Ti-12Mo alloy. This finding indicates that the combination of a temperature equals to 350 °C, a strain rate around 10^{-4} s^{-1} and Mo content close to 12 wt% results in the

highest intensity of PLC effect among all the tested conditions.

Fig. 7. Summary of serration types (a) and maximum stress drop magnitude $\Delta\sigma_{max}$ (b) in the

temperature range of 250-350 □ with strain rates from 10^{-3} s^{-1} down to 10^{-4} s^{-1}.

4.3 Overall evaluation of average stress drop magnitude

Fig. 8(a) shows the 3D surface plot with projection map of average stress drop magnitude

($\Delta\sigma_{average}$) for various Mo contents and engineering strains under the experimental condition (350 °C &

10^{-4} s^{-1}), with $\Delta\sigma_{average}=\Sigma(\Delta\sigma)/n$, as defined by Wang et al. [74], where n means the stress drop number

and $\Delta\sigma$ denotes the stress drop magnitude. Like $\Delta\sigma_{max}$, it can be seen that $\Delta\sigma_{average}$ also increases sharply

followed by a gradual decrease as Mo content increases from 10 wt% to 18 wt% at various engineering

strains. Moreover, for the other experimental conditions, similar trends are found though the results are

not given here. Furthermore, Fig. 8(b) shows a contour plot with some fundamental evolution

characteristics of $\Delta\sigma_{average}$ value. It can be found that the maximum $\Delta\sigma_{average}$ value (about 47 MPa) at

the engineering strain of 0.03 is approximately 1.5 times larger than the one at the engineering strain of

0.09, which is opposite to the result in Al-Mg alloy reported by Amokhtar et al. [41]. This is mainly

because the reconstruction rate of ω phase particles is lower than the destruction rate during the tensile

process. In addition, $\Delta\sigma_{average}$ evolution characteristics for different Mo contents are compared, as

shown in Fig. 8(b). It is clearly evident that $\Delta\sigma_{average}$ values of Mo contents (10, 12 and 15 wt%)

decrease almost linearly with increasing engineering strain. However, $\Delta\sigma_{average}$ evolution of Mo content

(18 wt%) shows an opposite trend, and its overall level is much lower compared to the other Mo

contents. This is mainly because a relatively lower ω phase fraction caused by high Mo content leads to

a smaller stress drop magnitude at the initial stage of deformation process in Ti-18Mo alloy. As the

experiment continues, the fraction of ω phase particles becomes larger because the low strain rate

provides a long ageing time for their precipitation. This will enhance ω precipitate-mobile dislocation

interactions, further leading to a slight increase of $\Delta\sigma_{average}$ value during the isothermal tensile process

in Ti-18Mo alloy. This explanation is directly supported by the ω reflection intensity of SAED patterns

as presented in Fig. 5, which is much lower than the ones for the other compositions and the same

experimental condition (350 °C & 10^{-4} s^{-1}). In other words, contrarily to the other three alloys, the

reconstruction rate of ω phase is higher compared with the destruction rate in Ti-18Mo alloy, even if

the final fraction of ω phase is the lowest one of all investigated Ti-xMo alloys.
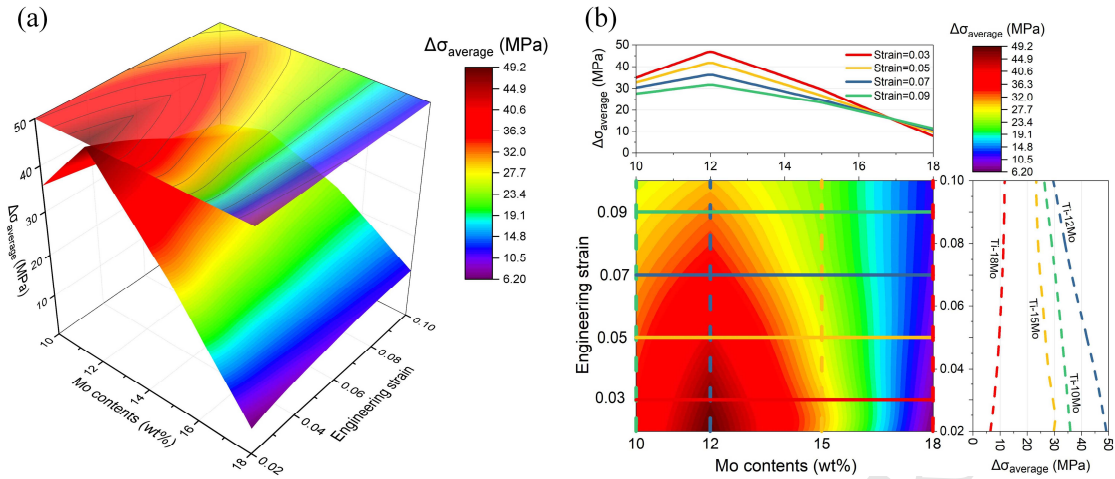
Fig. 8. 3D surface plot with projection map (a) and the contour plot with some fundamental evolution characteristics of average stress drop magnitude (b) at various Mo contents and engineering strains under the experimental condition (350 °C & 10^{-4} s^{-1}).

5. Conclusions

In the present paper, the thermo-mechanical properties and PLC effect of Ti-xMo alloys (x=10, 12, 15 and 18 wt%), in the temperature range of 250-350 °C and strain rates from 10^{-3} s^{-1} to 10^{-4} s^{-1}, are investigated in details and compared, along with the characterization of the microstructure after tension by TEM. The following conclusions are achieved:

(1) The value of Young modulus decreases with increasing Mo contents under all the experimental conditions, which is attributed to a more stable β phase matrix. Moreover, the highest values of Young modulus and 0.2% offset yield strength at elevated temperature are lower than the ones at room temperature in Ti-18Mo alloy, which are opposite to the results for the other three compositions. Their values also increase with decreasing strain rate. These trends are explained by the combined effects of temperature softening and ω phase strengthening. Precipitation of ω phase after tensile process is evidenced by TEM and its fraction is the lowest for the Ti-18Mo alloy among all the Ti-xMo alloys.

(2) Four kinds of serrated flow including types A, A+B, B and C are found at different temperatures and strain rates, corresponding to different propagation characteristics of PLC bands in Ti-xMo alloys. Moreover, increasing temperature and decreasing strain rate as well as Mo content result in the switch of the serration type from A to A+B, then to B and eventually to C, leading to the appearance of type C in Ti-10Mo and Ti-12Mo alloys under the experimental condition (350 °C & 10^{-4} s^{-1}). The above findings indicate that the spatial coupling force of PLC bands is weakened with the increase of temperature and the decrease of strain rate at a relatively lower Mo content, which is related to the strengthening intensity of ω precipitate-dislocation interactions.

(3) PLC effect occurs at elevated temperatures in Ti-xMo alloys, and the peak of maximum stress drop magnitude appears in Ti-12Mo alloy which is related to the volume fraction of ω phase particles. Moreover, the maximum stress drop magnitude increases with decreasing strain rate, because a relatively lower strain rate can reduce dislocations movement and provide a longer ageing time for the precipitation of ω phase particles, thereby leading to stronger ω precipitate-dislocation interactions. Furthermore, the average stress drop magnitude increases in Ti-18Mo alloy and decreases for the other three compositions as increasing engineering strain, depending on the fraction of ω phase particles.

References

[1] S. Joseph, I. Bantounas, T.C. Lindley, D. Dye, Slip transfer and deformation structures resulting from the low cycle fatigue of near-alpha titanium alloy Ti-6242Si, Int. J. Plast. 100 (2018) 90-103.

[2] J. Ruzic, S. Emura, X. Ji, I. Watanabe, Mo segregation and distribution in Ti-Mo alloy investigated using nanoindentation, Mater. Sci. Eng. A 718 (2018) 48-55.

[3] S.Y. Luo, D.H. Zhu, L. Hua, D.S. Qian, S.J. Yan, Numerical analysis of die wear characteristics in hot forging of titanium alloy turbine blade, Int. J. Mech. Sci. 123 (2017) 260-270.

[4] P. Castany, T. Gloriant, F. Sun, F. Prima, Design of strain-transformable titanium alloys, C. R. Phys. 19 (2018) 710-720.

[5] M.F. Ijaz, D. Laillé, L. Héraud, D.M. Gordin, P. Castany, T. Gloriant, Design of a novel superelastic Ti-23Hf-3Mo-4Sn biomedical alloy combining low modulus, high strength and large recovery strain, Mater. Lett. 177 (2016) 39-41.

[6] Y.M. Zhu, S.M. Zhu, M.S. Dargusch, J.F. Nie, HAADF-STEM study of phase separation and the subsequent α phase precipitation in a β-Ti alloy, Scr. Mater. 112 (2016) 46-49.

[7] P. Castany, D.M. Gordin, S.I. Drob, C. Vasilescu, V. Mitran, A. Cimpean, T. Gloriant, Deformation Mechanisms and Biocompatibility of the Superelastic Ti-23Nb-0.7Ta-2Zr-0.5N Alloy, Shape Mem. and Superelasticity 2 (2016) 18-28.

[8] H.Y. Zhan, G. Wang, D. Kent, M. Dargusch, The dynamic response of a metastable β Ti-Nb alloy to high strain rates at room and elevated temperatures, Acta Mater. 105 (2016) 104-113.

[9] X. Ji, S. Emura, X.H. Min, K. Tsuchiya, Strain-rate effect on work-hardening behavior in β-type Ti-10Mo-1Fe alloy with TWIP effect, Mater. Sci. Eng. A 707 (2017) 701-707.

[10] K. Endoh, M. Tahara, T. Inamura, H. Hosoda, Effect of Sn and Zr addition on the martensitic

22

transformation behavior of Ti-Mo shape memory alloys, J. Alloys Compd. 695 (2017) 76-82.

[11] Y.F. Zheng, D. Banerjee, H.L. Fraser, A nano-scale instability in the β phase of dilute Ti-Mo alloys, Scr. Mater. 116 (2016) 131-134.

[12] L.C. Campanelli, F.G. Coury, Y.F. Guo, P.S.C.P.D. Silva, M.J. Kaufman, C. Bolfarini, The role of twinning and nano-crystalline ω phase on the fatigue behavior of the metastable β Ti-15Mo alloy, Mater. Sci. Eng. A 729 (2018) 323-330.

[13] S. Banerjee, U.M. Naik, Plastic instability in an omega forming Ti-15% Mo alloy, Acta Mater. 44 (1996) 3667-3677.

[14] N.T.C. Oliveira, G. Aleixo, R. Caram, A.C. Guastaldi, Development of Ti-Mo alloys for biomedical applications: Microstructure and electrochemical characterization, Mater. Sci. Eng. A 452-453 (2007) 727-731.

[15] P.B Vila, V.B. Oliveira, S. Schwarz, T. Buslaps, G. Requena, Tracking the α″ martensite decomposition during continuous heating of a Ti-6Al-6V-2Sn alloy, Acta Mater. 135 (2017) 132-143.

[16] X.H. Min, S. Emura, K. Tsuchiya, T. Nishimura, K. Tsuzaki, Transition of multi-deformation modes in Ti-10Mo alloy with oxygen addition, Mater. Sci. Eng. A 590 (2014) 88-96.

[17] P. Samimi, Y. Liu, I. Ghamarian, P.C. Collins, A novel tool to assess the influence of alloy composition on the oxidation behavior and concurrent oxygen-induced phase transformations for binary Ti-xMo alloys at 650 °C, Corros. Sci. 89 (2014) 295-306.

[18] W.F. Ho, C.P. Ju, J.H.C. Lin, Structure and properties of cast binary Ti-Mo alloys, Biomaterials 20 (1999) 2115-2122.

[19] X.F. Zhao, M. Niinomi, M. Nakai, J. Hieda, Beta type Ti-Mo alloys with changeable Young's

modulus for spinal fixation applications, Acta Biomater. 8 (2012) 1990-1997.

[20] W.F. Ho, Effect of omega phase on mechanical properties of Ti-Mo alloys for biomedical applications, J. Med. Biol. Eng. 28 (2008) 47-51.

[21] Y.L. Zhou, D.M. Luo, Microstructures and mechanical properties of Ti-Mo alloys cold-rolled and heat treated, Mater. Charact. 62 (2011) 931-937.

[22] F. Sun, J.Y. Zhang, M. Marteleur, T. Gloriant, P. Vermaut, D. Laillé, P. Castany, C. Curfs, P.J. Jacques, F. Prima, Investigation of early stage deformation mechanisms in a metastable β titanium alloy showing combined twinning-induced plasticity and transformation-induced plasticity effects, Acta Mater. 61 (2013) 6406-6417.

[23] F.F. Cardoso, P.L. Ferrandini, E.S.N. Lopes, A. Cremasco, R. Caram, Ti-Mo alloys employed as biomaterials: Effects of composition and aging heat treatment on microstructure and mechanical behavior, J. Mech. Behav. Biomed. Mater. 32 (2014) 31-38.

[24] F. Prima, P. Vermaut, T. Gloriant, J. Debuigne, D. Ansel, Experimental evidence of elastic interaction between ω nanoparticles embedded in a metastable β titanium alloy, J. Mater. Sci. Lett. 21 (2002) 1935-1937.

[25] J. Debuigne, F. Prima, Growth kinetic model for isothermal omega phase particles in low-cost beta titanium Ti-6.8 Mo-4.5 Fe-1.5 Al alloy, Mater. Trans. 46 (2005) 1433-1435.

[26] F. Sun, D. Laillé, T. Gloriant, Thermal analysis of the ω nanophase transformation from the metastable β Ti–12Mo alloy, J. Therm. Anal. Calorim. 101 (2010) 81-88.

[27] W.D. Zhang, Y. Liu, H. Wu, M. Song, T.Y. Zhang, X.D. Lan, T.H. Yao, Elastic modulus of phases in Ti-Mo alloys, Mater. Charact. 106 (2015) 302-307.

[28] X. Lu, B. Sun, T.F. Zhao, L.N. Wang, C.C. Liu, X.H. Qu, Microstructure and mechanical

properties of spark plasma sintered Ti-Mo alloys for dental applications, Int. J. Min. Met. Mater. 21 (5) 479-486.

[29] C.M. Lee, C.P. Ju, J.H.C. Lin, Structure-property relationship of cast Ti-Nb alloys, J. Oral Rehabil. 29 (2002) 314-322.

[30] H.Y. Kim, Y. Ikehara, J.I. Kim, H. Hosoda, S. Miyazaki, Martensitic transformation, shape memory effect and superelasticity of Ti-Nb binary alloys, Acta Mater. 54 (2006) 2419-2429.

[31] F. Sun, F. Prima, T. Gloriant, High-strength nanostructured Ti-12Mo alloy from ductile metastable beta state precursor, Mater. Sci. Eng. A 527 (2010) 4262-4269.

[32] X.H. Min, S. Emura, L. Zhang, K. Tsuzaki, K. Tsuchiya, Improvement of strength-ductility tradeoff in β titanium alloy through pre-strain induced twins combined with brittle ω phase, Mater. Sci. Eng. A 646 (2015) 279-287.

[33] A. Portevin, F. Le Chatelier, Sur un phénomène observé lors de l'essai de traction d'alliages en cours de transformation, Seanc. Acad. Sci. Paris 176 (1923) 507-510.

[34] H. Zhong, P.A. Rometsch, Q.Q. Zhu, L.F. Cao, Y. Estrin, Influence of pre-ageing on the stretch formability of Al-Mg-Si automotive sheet alloys, Mater. Sci. Eng. A 687 (2017) 323-331.

[35] Y.L. Cai, C.G. Tian, S.H. Fu, G.M. Han, C.Y. Cui, Influence of γ′ precipitates on Portevin-Le Chatelier effect of Ni-based superalloys, Mater. Sci. Eng. A 638 (2015) 314-321.

[36] H.W. Zhou, J.F. Fang, Y. Chen, L. Yang, H. Zhang, Y. Lu, Y.Z. He, Internal friction studies on dynamic strain aging in P91 ferritic steel, Mater. Sci. Eng. A 676 (2016) 361-365.

[37] K. Prasad, A. Amrithapandian, B.K. Panigrahi, V. Kumar, K.B.S. Rao, M. Sundararaman, Experimental evidence for segregation of interstitial impurities to defects in a near α titanium alloy during dynamic strain aging using energy filtered transmission electron microscopy, Mater.

Sci. Eng. A 638 (2015) 90-96.

[38] X.Y. Fang, D.Q. Yi, J.F. Nie, The serrated flow behavior of Mg-Gd (-Mn-Sc) alloys, Metall. Mater. Trans. A 40 (2009) 2761-2770.

[39] E. Pink, The effect of precipitates on characteristics of serrated flow in AlZn5Mg1, Acta Metall. 37 (1989) 1773-1781.

[40] B.J Brindley, P.J. Worthington, Serrated yielding in aluminium-3% magnesium, Acta Metall. 17 (1969) 1357-1361.

[41] H.A. Amokhtar, C. Fressengeas, K. Bouabdallah, On the effects of the Mg content on the critical strain for the jerky flow of Al-Mg alloys, Mater. Sci. Eng. A 631 (2015) 209-2013.

[42] Y.L. Cai, S.L. Yang, S.H. Fu, D. Zhuang, Q.C. Zhang, Investigation of Portevin-Le Chatelier band strain and elastic shrinkage in Al-based alloys associated with Mg contents, J. Mater. Sci. Technol. 33 (2017) 580-586.

[43] A.A. Shibkov, A.A. Denisov, M.A. Zheltov, A.E. Zolotov, M.F. Gasanov, The electric current-induced suppression of the Portevin-Le Chatelier effect in Al-Mg alloys, Mater. Sci. Eng. A 610 (2014) 338-343.

[44] S.Z. Niu, H.C. Kou, Y. Zhang, J. Wang, J.S. Li, The characteristics of serration in $Al_{0.5}CoCrFeNi$ high entropy alloy, Mater. Sci. Eng. A 702 (2017) 96-103.

[45] P.Y. Manach, S. Thuillier, J.W. Yoon, J. Coër, H. Laurent, Kinematics of Portevin-Le Chatelier bands in simple shear, Int. J. Plast. 58 (2014) 66-83.

[46] M.N. Gussev, N. Sridharan, M. Norfolk, K.A. Terrani, S.S. Babu, Effect of post weld heat treatment on the 6061 aluminum alloy produced by ultrasonic additive manufacturing, Mater. Sci. Eng. A 684 (2017) 606-616.

[47] Y.L. Cai, S.L. Yang, Y.H. Wang, S.H. Fu, Q.C. Zhang, Characterization of the deformation behaviors associated with the serrated flow of a 5456 Al-based alloy using two orthogonal digital image correlation systems, Mater. Sci. Eng. A 664 (2016) 155-164.

[48] A.B. Spierings, K. Dawson, K. Kern, F. Palm, K. Wegener, SLM-processed Sc- and Zr- modified Al-Mg alloy: Mechanical properties and microstructural effects of heat treatment, Mater. Sci. Eng. A 701 (2017) 264-273.

[49] Q.C. Zhang, Z.Y. Jiang, H.F. Jiang, Z.J. Chen, X.P. Wu, On the propagation and pulsation of Portevin-Le Chatelier deformation bands: An experimental study with digital speckle pattern metrology, Int. J. Plast. 21 (2005) 2150-2173.

[50] D. Delpueyo, X. Balandraud, M. Grédiac, Calorimetric signature of the Portevin-Le Châtelier effect in an aluminum alloy from infrared thermography measurements and heat source reconstruction, Mater. Sci. Eng. A 651 (2016) 135-145.

[51] S.H. Fu, G. Yue, Y.L. Cai, T. Cheng, Q.C. Zhang, X.P. Wu, Study on the out-of-plane deformation of the Portevin-Le Chatelier band by using digital shearography, Measurement 72 (2015) 61–67.

[52] L. Casarotto, H. Dierke, R. Tutsch, H. Neuhäuser, On nucleation and propagation of PLC bands in an Al-3Mg alloy, Mater. Sci. Eng. A 527 (2009) 132-140.

[53] K. Chihab, Y. Estrin, L.P. Kubin, J. Vergnol, The kinetics of the Portevin-Le Chatelier bands in an Al-5at%Mg alloy, Scr. Metall. 21 (1987) 203-208.

[54] D. Yuzbekova, A. Mogucheva, D. Zhemchuzhnikova, T. Lebedkina, M. Ledyodkin, R. Kaibyshev, Effect of microstructure on continuous propagation of the Portevin-Le Chatelier deformation bands, Int. J. Plast. 96 (2017) 210-226.

[55] R. Shabadi, S. Kumar, H.J. Roven, E.S. Dwarakadasa, Characterisation of PLC band parameters

using laser speckle technique, Mater. Sci. Eng. A 364 (2004) 140-150.

[56] M. Callahan, O. Hubert, F. Hild, A. Perlade, J.H. Schmitt, Coincidence of strain-induced TRIP and propagative PLC bands in Medium Mn steels, Mater. Sci. Eng. A 704 (2017) 391-400.

[57] F. Yang, H.W. Luo, E.X. Pu, S.L. Zhang, H. Dong, On the characteristics of Portevin-Le Chatelier bands in cold-rolled 7Mn steel showing transformation-induced plasticity, Int. J. Plast. 103 (2018) 188-202.

[58] X.G. Wang, L. Wang, M.X. Huang, Kinematic and thermal characteristics of Lüders and Portevin-Le Châtelier bands in a medium Mn transformation-induced plasticity steel, Acta Mater. 124 (2017) 17-29.

[59] X.D. Bian, F.P. Yuan, X.L. Wu, Correlation between strain rate sensitivity and characteristics of Portevin-Le Chátelier bands in a twinning-induced plasticity steel, Mater. Sci. Eng. A 696 (2017) 220-227.

[60] S.T. Zhao, C.L. Meng, F.X. Mao, W.P. Hu, G. Gottstein, Influence of severe plastic deformation on dynamic strain aging of ultrafine grained Al-Mg alloys, Acta Mater. 76 (2014) 54-67.

[61] D.A. Zhemchuzhnikova, M.A. Lebyodkin, T.A. Lebedkina, R.O. Kaibyshev, Unusual behavior of the Portevin-Le Chatelier effect in an AlMg alloy containing precipitates, Mater. Sci. Eng. A 639 (2015) 37-41.

[62] D. Zhemchuzhnikova, M. Lebyodkin, D. Yuzbekova, T. Lebedkina, A. Mogucheva, R. Kaibyshev, Interrelation between the Portevin Le-Chatelier effect and necking in AlMg alloys, Int. J. Plast. 10 (2018) 95-109.

[63] K. Gopinath, A.K. Gogia, S.V. Kamat, U. Ramamurty, Dynamic strain ageing in Ni-base superalloy 720Li, Acta Mater. 54 (2009) 1243-1253.

[64] Y.L. Cai, C.G. Tian, G.L. Zhang, G.M. Han, S.L. Yang, S.H. Fu, C.Y. Cui, Q.C. Zhang, Influence of γ′ precipitates on the critical strain and localized deformation of serrated flow in Ni-based superalloys, J. Alloy. Compd. 690 (2017) 707-715.

[65] L. Yuan, X.Y. Gao, X.Q. Zhang, Y.A. Yang, Mechanical properties and Portevin-Le Châtelier effect of a Ni-Cr-Mo alloy containing ordered phase with Pt_2Mo-type structure at elevated temperature, Mater. Sci. Eng. A 680 (2017) 115-120.

[66] R.J. Grylls, S. Banerjee, S. Perungulam, R. Wheeler, H.L. Fraser, On the discontinuous yielding phenomena observed in a Nb-Ti-Al alloy, Intermetallics 6 (1998) 749-752.

[67] D. Choudhuri, S.A. Mantri, T. Alam, S. Banerjee, R. Banerjee, Precipitate-dislocation interaction mediated Portevin-Le Chatelier-like effect in a beta-stabilized Ti-Mo-Nb-Al alloy, Scr. Mater. 124 (2016) 15-20.

[68] S.A. Mantri, D. Choudhuri, T. Alam, V. Ageh, F. Sun, F. Prima, R. Banerjee, Change in the deformation mode resulting from beta-omega compositional partitioning in a Ti-Mo alloy: Room versus elevated temperature, Scr. Mater. 130 (2017) 69-73.

[69] S.Y. Luo, P. Castany, S. Thuillier, M. Huot, Spatiotemporal characteristics of Portevin-Le Chatelier effect in Ti-Mo alloys under thermo-mechanical loading, Mater. Sci. Eng. A 733 (2018) 137-143.

[70] A. Gysler, G. Lütjering, V. Gerold, Deformation behavior of age-hardened Ti-Mo alloys, Acta Metall. 22 (1974) 901-909.

[71] A. Almeida, D. Gupta, C. Loable, R. Vilar, Laser-assisted synthesis of Ti-Mo alloys for biomedical applications, Mater. Sci. Eng. C 32 (2012) 1190-1195.

[72] X.H. Min, K. Tsuzaki, S. Emura, K. Tsuchiya, Enhancement of uniform elongation in high

strength Ti-Mo based alloys by combination of deformation modes, Mater. Sci. Eng. A 528 (2011) 4569-4578.

[73] C.H. Wang, C.D. Yang, M. Liu, X. Li, P.F. Hu, A.M. Russell, G.H. Cao, Martensitic microstructures and mechanical properties of as-quenched metastable β-type Ti-Mo alloys, J. Mater. Sci. 51 (2016) 6886-6896.

[74] W.H. Wang, D. Wu, S.S.A. Shah, R.S. Chen, C.S. Lou, The mechanism of critical strain and serration type of the serrated flow in Mg-Nd-Zn alloy, Mater. Sci. Eng. A 649 (2016) 214-221.